

Hybrid Heterostructures of a Spin Crossover Coordination Polymer on MoS₂: Elucidating the Role of the 2D Substrate

Alejandro Núñez-López, Ramón Torres-Cavanillas, Marc Morant-Giner, Natalia Vassilyeva, Richard Mattana, Sergio Tatay, Philippe Ohresser, Edwige Otero, Emiliano Fonda, Michael Paulus, Víctor Rubio-Giménez, Alicia Forment-Aliaga,* and Eugenio Coronado*


Controlling the deposition of spin-crossover (SCO) materials constitutes a crucial step for the integration of these bistable molecular systems in electronic devices. Moreover, the influence of functional surfaces, such as 2D materials, can be determinant on the properties of the deposited SCO film. In this work, ultrathin films of the SCO Hofmann-type coordination polymer [Fe(py)₂{Pt(CN)₄}] (py = pyridine) onto monolayers of 1T and 2H MoS₂ polytypes are grown. The resulting hybrid heterostructures are characterized by GIXRD, XAS, XPS, and EXAFS to get information on the structure and the specific interactions generated at the interface, as well as on the spin transition. The use of a layer-by-layer results in SCO/2D heterostructures, with crystalline and well-oriented [Fe(py)₂{Pt(CN)₄}]. Unlike with conventional Au or SiO₂ substrates, no intermediate self-assembled monolayer is required, thanks to the surface S atoms. Furthermore, it is observed that the higher presence of Fe³⁺ in the 2H heterostructures hinders an effective spin transition for [Fe(py)₂{Pt(CN)₄}] films thinner than 8 nm. Remarkably, when using 1T MoS₂, this transition is preserved in films as thin as 4 nm, due to the reducing character of this metallic substrate. These results highlight the active role that 2D materials play as substrates in hybrid molecular/2D heterostructures.

1. Introduction

The spin crossover (SCO) phenomenon is one of the most spectacular examples of molecular bistability. It is displayed by some coordinated d-transition metal ions with d⁴ to d⁷ configuration. These metal complexes may exist in low-spin (LS) or high-spin (HS) electronic states, which can be switched by applying external stimuli like temperature, light, or pressure.^[1] Furthermore, these states exhibit entirely different physical properties (mechanical, optical, thermal, etc.),^[2-4] allowing the use of SCO compounds as molecular components in hybrid electronic devices with sensing, actuating, or memory capabilities.^[5-7] Different processing routes have been developed in the past few years to incorporate them in these nanodevices while controlling their morphology, thickness, and crystallinity.^[8] In this regard, SCO complexes that can be grown layer-by-layer (LbL) are particularly interesting since their thickness

A. Núñez-López, R. Torres-Cavanillas, M. Morant-Giner, N. Vassilyeva, S. Tatay, V. Rubio-Giménez, A. Forment-Aliaga, E. Coronado
Instituto de Ciencia Molecular (ICMol)
Universitat de València
46980, Catedrático José Beltrán 2 Paterna, Spain
E-mail: alicia.forment@uv.es; eugenio.coronado@uv.es
R. Torres-Cavanillas
Department of Materials
University of Oxford
OX1 3PH Oxford, UK
M. Morant-Giner
Department of Chemical and Pharmaceutical Sciences
University of Trieste
34127, Via L. Giorgieri 1 Trieste, Italy

R. Mattana
Unité Mixte de Physique, CNRS, Thales
Université Paris-Saclay
91767 Palaiseau, France
P. Ohresser, E. Otero, E. Fonda
Synchrotron SOLEIL
L'Orme des Merisiers
91190 Saint Aubin, France
M. Paulus
Fakultät Physik/DELTA
Technische Universität Dortmund
44221 Dortmund, Germany
V. Rubio-Giménez
Centre for Membrane Separations, Adsorption, Catalysis and Spectroscopy (cMACS)
Katholieke Universiteit Leuven
Celestijnenlaan 200F, Leuven 3001, Belgium

 The ORCID identification number(s) for the author(s) of this article can be found under <https://doi.org/10.1002/smll.202304954>

© 2023 The Authors. Small published by Wiley-VCH GmbH. This is an open access article under the terms of the Creative Commons Attribution-NonCommercial License, which permits use, distribution and reproduction in any medium, provided the original work is properly cited and is not used for commercial purposes.

DOI: 10.1002/smll.202304954

and morphology can be easily controlled, ranging from nanometric to micrometric films. An archetypical example is provided by the SCO Hofmann-type coordination polymer (HTCP) $[\text{Fe}(\text{py})_2\{\text{Pt}(\text{CN})_4\}]$ (py = pyridine),^[9] as it presents a layered-like structure, facilitating its LbL growth at room temperature and under a controlled atmosphere, in contrast with other HTCP, which can only be prepared at very low temperatures.^[10] Additionally, this HTCP exhibits a spin transition centered at 205 K which remains detectable down to 7 layers when grown on metallic substrates.^[11,12] However, the development of smaller and thinner SCO nanodevices is still hampered by the loss of the spin transition when the SCO complex is in direct contact with the substrate. For this reason, recent works have focused on studying the interaction between different substrates and the SCO material.^[13] For instance, in the SCO molecule $[\text{Fe}(\text{H}_2\text{B}(\text{pz})_2)_2(\text{phen})]$ deposited on Au (111) a full blocking of the LS state occurs for the first layer,^[14,15] while when anchored on Bi (111) it exhibits a partial HS blocking.^[16] A second example is provided by the related molecule $[\text{Fe}(\text{H}_2\text{B}(\text{pz})_2)_2(\text{bpy})]$. In this case, for thin films deposited on the organic ferroelectric copolymer polyvinylidene fluoride-trifluoroethylene (PVFT), a HS state is stabilized when the PVFT dipole is pointing “up,” while the LS is fixed for the “down” dipole orientation.^[17] These results indicate that the spin-switching capabilities of the device are strongly affected by the nature of the substrate and, in particular, by the interactions established at the hybrid interface.

In this context, using 2D materials as substrates provides a unique opportunity to study the hybrid molecular/inorganic interface in detail since all the 2D material belongs to the interface. Taking advantage of this feature, several SCO/2D heterostructures have been prepared to sense the spin transition of the SCO component through the change detected in the electrical or optical properties of the 2D material. For instance, some works have explored the manipulation of graphene electrical properties by preparing heterostructures based on SCO nanoparticles,^[18,19] crystals,^[20,21] or evaporated films.^[22,23] Other works have exploited the change experienced in the optical properties (photoluminescence) of 2D semiconductors, such as 2H MoS₂ or WSe₂ monolayers, to sense the strain induced on them by the spin transition.^[21,24] Notice that all these previous works were focused on studying the change experienced in the properties of the 2D material by the influence of the SCO component. The complementary question, i.e., how the 2D material affects the properties of the SCO component, has not been investigated so far.^[25,26]

Herein, we address this question by using two different MoS₂ polytypes as the 2D material. In nature, this transition metal dichalcogenide is found in the hexagonal 2H polytype with a trigonal prismatic Mo coordination that behaves as an indirect bandgap semiconductor. However, once exfoliated down to the monolayer, it may maintain the 2H polytype, becoming a direct bandgap semiconductor with strong photoluminescence (PL), or change into the 1T phase, with an octahedral coordination geometry and metallic behavior.^[27] This 1T phase is metastable and may undergo structural distortions to yield other nonstable polytypes.^[28–32] Furthermore, what makes MoS₂ so interesting is the fact that its physical properties and polytypes can be easily tuned by doping, chemical functionalization, strain, or other external effects.^[33–36] In our case, we focus on creating a hybrid heterostructure with the SCO component HTCP $[\text{Fe}(\text{py})_2\{\text{Pt}(\text{CN})_4\}]$.

This coordination polymer was directly grown onto 1T and 2H MoS₂ flakes, previously prepared by chemical exfoliation and deposition on a SiO₂ substrate. The HTCP was grown using a bottom-up LbL methodology, which permits the complete coverage of the exposed side of the 2D material with the SCO component and gives rise to a Janus SCO/2D heterostructure.^[18,20,22,37] The advanced characterization of these hybrid heterostructures was performed by using X-ray absorption spectroscopy (XAS), X-ray photoelectron spectroscopy (XPS), and extended X-ray fine structure (EXAFS). These techniques provided key information on the specific interactions generated at the interface, as well as on the spin transition. They showed that when using 1T MoS₂ flakes, the spin transition is preserved in SCO films as thin as 4 nm (5 layers) thanks to the reducing character of this metallic substrate, which prevents the Fe²⁺ from oxidation, while for 2H MoS₂ thicker SCO films (larger than 8 nm) are required.

2. Results and Discussion

2.1. Synthesis of the HTCP/MoS₂ Heterostructures

The first step involves the exfoliation and isolation of 1T or 2H MoS₂ layers from the bulk. To obtain the 1T MoS₂ polytype, the exfoliation is carried out using the *n*-BuLi intercalation method,^[38] which leads to an aqueous colloid of negatively charged exfoliated MoS₂ due to the electron donation from the *n*-BuLi (Figure S1, Supporting Information). Then, the 1T MoS₂ is spin-coated on a SiO₂ substrate to form a well-packed network of MoS₂ ultrathin layers with an average height of 1.5 ± 0.3 nm, as shown by the atomic force microscopy (AFM) images (Figure S2, Supporting Information). To obtain the 2H MoS₂ polytype, the previously prepared 1T MoS₂ network deposited on SiO₂ is heated at 200 °C for 1 h under an inert atmosphere (Figure S3, Supporting Information).^[39] This process leads to an almost complete conversion from 1T to 2H, as shown by the Mo 3d XPS spectra (Figure S4, Supporting Information) and Raman spectroscopy (Figure S5, Supporting Information).^[39] It must be noted that the thickness of the converted 2H phase remains similar to the 1T polytype (0.9 ± 0.7 nm, Figure S6, Supporting Information). Next, via an optimized LbL protocol (Figure 1a), we proceed to grow the HTCP on the 2D network of the two MoS₂ polytypes (HTCP/1T and HTCP/2H, Figure 1b). The strategy is based on the successive immersion of the MoS₂-covered substrates in an ethanolic solution of Fe²⁺ and the py ligand followed by another solution of (TBA)₂Pt(CN)₄ (TBA = tetrabutylammonium) with intermediate washing steps in pure ethanol. The whole process is automated to ensure reproducibility and is performed under an inert atmosphere to minimize Fe²⁺ oxidation.^[12]

Next, we analyze the deposition of $[\text{Fe}(\text{py})_2\{\text{Pt}(\text{CN})_4\}]$ using AFM, scanning transmission electron microscopy (STEM), and energy dispersive X-ray spectroscopy (EDS). As shown in Figure 2a–c and Figures S7–S20 and Table S1 (Supporting Information), the HTCP grows preferentially on top of the flakes of both MoS₂ polytypes rather than on the exposed SiO₂ substrate with a Fe:Pt ratio close to 1, the calculated value from the chemical formula. AFM height distributions indicate a linear thickness increase of the whole HTCP/MoS₂ heterostructures with successive cycles. The growth per cycle was ≈ 0.74 and ≈ 0.78 nm for the 1T and 2H MoS₂ substrates, respectively. This is in good agreement

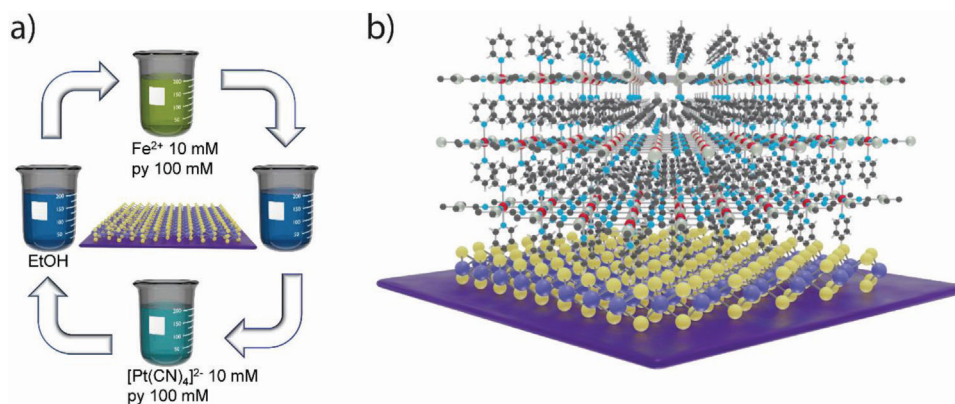


Figure 1. a) Schematic representation of the growth of $[\text{Fe}(\text{py})_2\{\text{Pt}(\text{CN})_4\}]$ by automated LbL on top of the MoS_2 flakes deposited onto a SiO_2 substrate. b) Schematic representation of the formed HTCP/ MoS_2 heterostructure. Color code: Mo (violet), S (yellow), Fe (maroon), Pt (silver), C (gray), and N (blue). H atoms are omitted for clarity.

with the crystallographic interlayer distance in $[\text{Fe}(\text{py})_2\{\text{Pt}(\text{CN})_4\}]$ (0.76 nm, Figure 2c), similar to its growth on Au substrates.^[11,12] This clearly supports that a single layer of HTCP grows directly on top of the MoS_2 flakes with each LbL immersion cycle. Notably, in the present case, no anchoring molecule is required to link the substrate and the target molecule or film. Thus, the first Fe^{2+} centers directly bind to the MoS_2 . This is in sharp contrast with the common procedure used to grow ultrathin films of extended coordination polymers on an inorganic substrate since it often requires the insertion of a molecular self-assembled monolayer (SAM) in between the two components to warrant the homogeneity of the film.^[12,40] We hypothesize that the direct growth of HTCP on MoS_2 occurs either via the coordination of Fe^{2+} ions by S lone pair at the MoS_2 basal plane or simply by electrostatic interactions between the positive ions and the negatively charged MoS_2 surface in the case of 1T MoS_2 . Nevertheless, the fact that the HTCP grows similarly in both MoS_2 substrates (1T is partially charged, while 2H is not) indicates that anchoring via S coordination is most likely. This facilitates the synthetic protocol and enhances the HTCP/ MoS_2 interaction. Then, these Fe^{2+} ions would act as nucleation centers for the subsequent formation of the pillared 2D layers by the alternate immersions in $\text{Pt}(\text{CN})_4^{2-}:\text{py}$

and $\text{Fe}^{2+}:\text{py}$ solutions. The morphology of the coordination compound evidences a grain structure, similar to previous results of LbL growth of HTCP on Au.^[11,12]

2.2. Characterization of the HTCP/ MoS_2 Heterostructures

When we analyze the chemical composition of the heterostructures by means of XPS, survey spectra (Figure S21, Supporting Information) show the presence of the main components (Fe, Pt, C, N, Mo, and S) in all cases. However, some relevant changes occur in the 1T MoS_2 Mo 3d edge after the HTCP growth (Figure 3a). Focusing on the bare 1T MoS_2 , the signal is fit to four doublets arising from Mo 3d 1T MoS_2 (purple), 2H MoS_2 (cyan), and MoO_2 (orange), and S 2s MoS_2 (green) contributions, see Table S2 (Supporting Information) for the values of each component. The presence of the cyan-colored band is due to a $\approx 16\%$ residual 2H MoS_2 in the exfoliated materials. After 7 cycles of HTCP growth, all the Mo 3d bands blue-shift by ≈ 0.4 eV but the sample maintain its 1T phase character, as confirmed by the presence of J peaks in Raman spectroscopy (Figure S22, Supporting Information). We ascribe this shift to the electron donation from the MoS_2

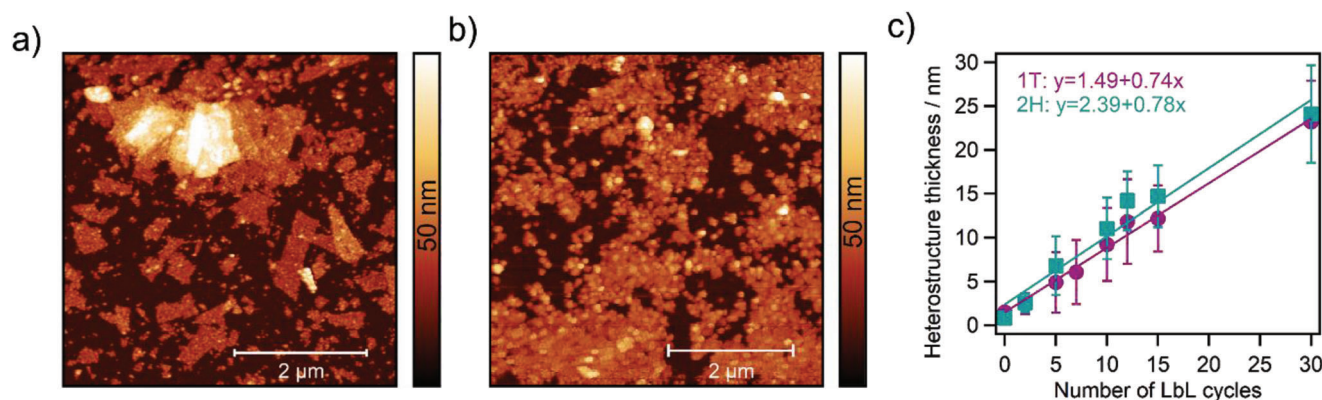


Figure 2. AFM topography of the heterostructure a) HTCP(x15)/1T and b) HTCP(x12)/2H. c) Linear dependence between the number of LbL immersion cycles and HTCP/ MoS_2 thickness.

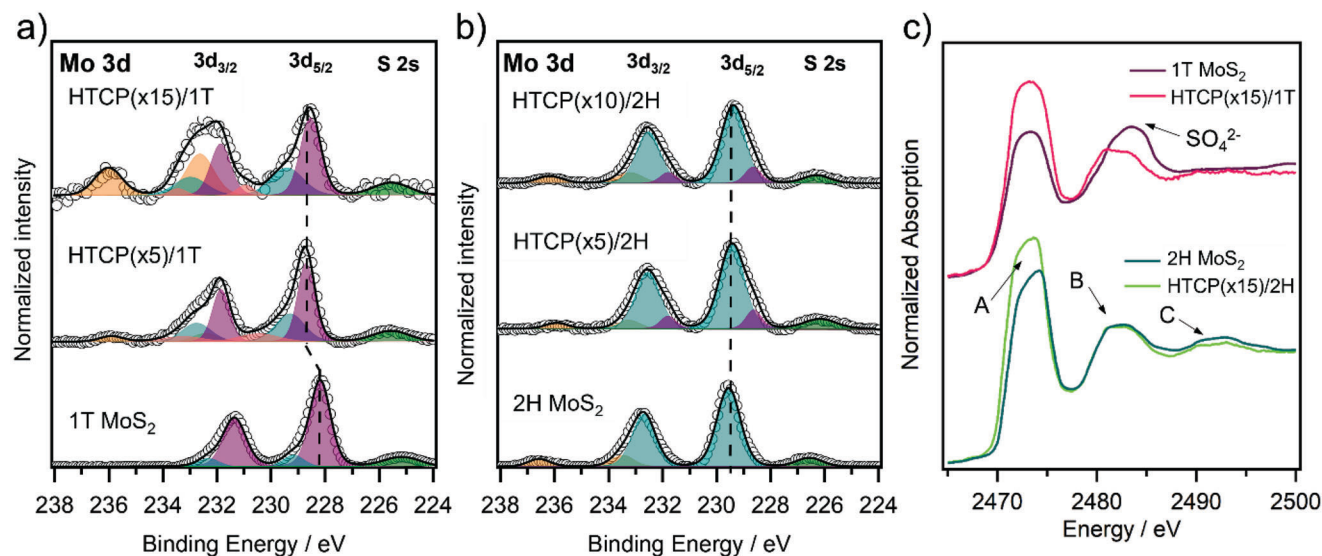


Figure 3. High-resolution XPS spectra of Mo 3d for the a) 1T MoS₂ and HTCP/1T heterostructures (5 and 10 cycles), and b) 2H MoS₂ and HTCP/2H heterostructures (5 and 15 cycles). c) S K-edge XAS of bare 1T and 2H MoS₂ and the heterostructures HTCP(x15)/MoS₂.

to the HTCP, affecting the MoS₂ work function, the Mo 3d levels, or both.^[41,42] This effect is associated with the reducing character of the 1T MoS₂ due to an excess of negative charge, which originated during the exfoliation protocol with *n*-BuLi. Thus, 1T MoS₂ is more reactive and prone to inducing charge transfer phenomenon. In contrast, this effect is not observed in the XPS spectra of the 2H MoS₂ heterostructures (Figure 3b), the Mo 3d bands are poorly affected upon the formation of the HTCP. Interestingly, looking at the S 2p region, a similar blue-shift is observed upon the functionalization of 1T MoS₂ (Figure S23 and Table S3, Supporting Information), supporting the electron donation from the MoS₂ to the HTCP.

In order to further explore the specific interactions between the MoS₂ and the HTCP observed by XPS, we have followed the S K-edge XAS and Mo K-edge XAS at 300 K. Starting with the S K-edge, 1T MoS₂ and 2H MoS₂ spectra of bulk samples (Figure 3c and Figure S24, Supporting Information) show clear differences between the 1T and 2H phases; these are mainly the shape of the A peak (related to the electron transition of S 1s electrons to unoccupied hybridized S 3p orbitals), the relative intensities of A and B peaks (being B related to the transition from S 1s electrons to antibonding p-like final states) and the presence of a third peak at higher energy in the case of the 2H polytype (C peak).^[43] Next, the S K-edge spectra of 2H and 1T heterostructures with different numbers HTCP layers are analyzed (Figures S25 and S26, Supporting Information). The peak positions of the 2H HTCP/MoS₂ samples at 300 K perfectly fit with the 2H reference sample. Nevertheless, there is an evident increase in the intensity of the A band. As there is no remarkable alteration of the S 2p XPS spectra, we attribute this change to an increase of S 3p unoccupied density of states due to the coordination of S to Fe²⁺ ions.^[44,45] The same A band modifications are observed in the 1T MoS₂ S K-edge, providing evidence of specific interactions at the interface where Fe ions in HTCP are coordinated by the lone pair of the S atoms in MoS₂. This coordination is fur-

ther confirmed by the valence band XPS of the heterostructure (Figure S27, Supporting Information).^[46,47] Therefore, eliminating the electrostatic interaction as the source of the Fe²⁺ anchoring. Remarkably, the broadening of the B band, attributed to the presence of some oxidized species (e.g., SO₄²⁻) is absent in the heterostructure due to the limited MoS₂ exposure and reactivity to air of 1T S atoms after the HTCP functionalization.^[48] Moving to the Mo K-edge XAS, which corresponds to the excitation from the Mo 1s to 5p orbitals, the bulk sample spectra show three peaks D, E, and F (Figure S28, Supporting Information). 1T MoS₂ layers present a less pronounced D peak, as can be seen in the inset of Figure S28a (Supporting Information). Focusing on the heterostructures, the spectrum of the reference 2H MoS₂ is matched in the HTCP/2H, while in the HTCP/1T some small changes in the intensity of the D peak are observed, supporting the electron withdrawal effect of 1T MoS₂ already observed by XPS in the Mo 3d region.

The chemical composition and electronic signature of the HTCP have been studied by infrared spectroscopy and XPS, while its crystallinity has been studied by synchrotron grazing incidence X-ray diffraction (GIXRD). The infrared reflection absorption spectra (IRRAS) of the films match perfectly with the Fourier-transform infrared (FT-IR) spectrum of the bulk material, showing all the characteristic vibrations of HTCP (Figure 4a). By monitoring the intensity of the C≡N (2173 cm⁻¹) and the py ring (1600–1000 cm⁻¹) stretching bands with the number of cycles, the sequential growth of the HTCP over the MoS₂ can be further confirmed (Figures S29–S32, Supporting Information).

Regarding the electronic signature of the HTCP, we explore the Fe 2p (Figure 4b) and Pt 4f (Figure S33, Supporting Information) regions of the XPS at 300 K in the two heterostructures. The interpretation of Fe oxidation state is far more complex due to satellite bands and multiple splitting features. Nevertheless, it is clear that the spectra of all the samples resemble each other

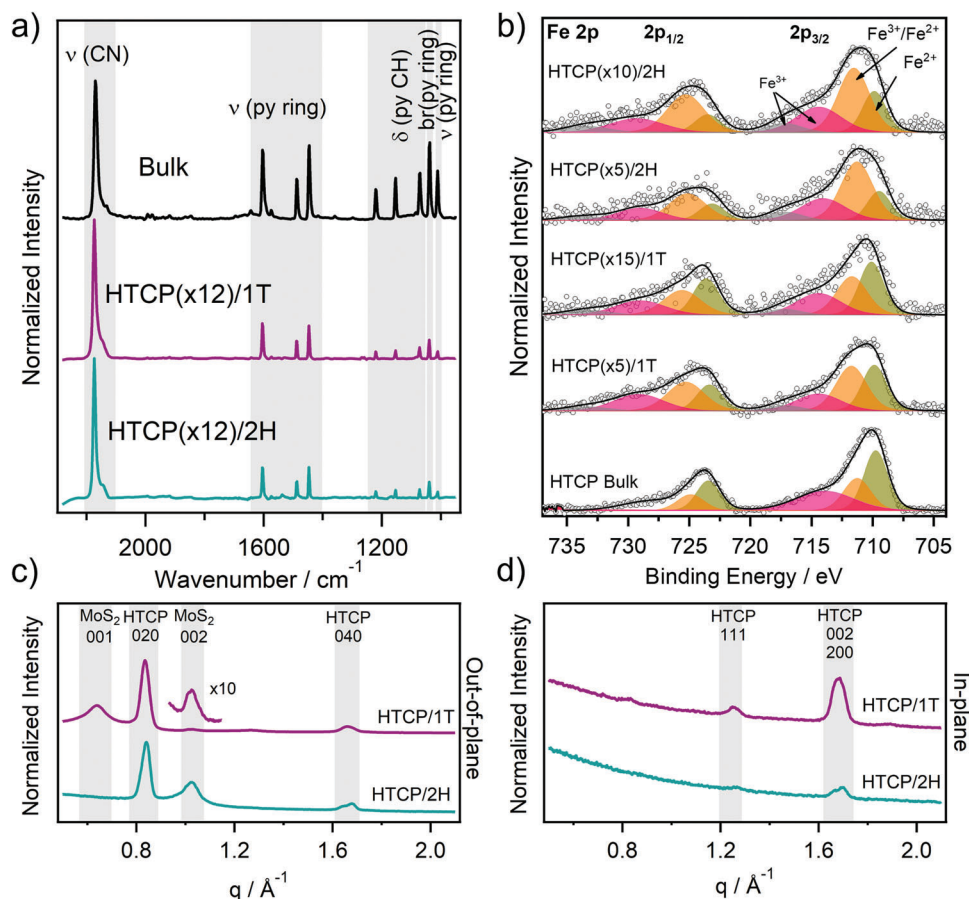


Figure 4. a) IRRAS spectra of the 1T and 2H heterostructures with 12 HTCP layers compared with the FT-IR spectra of the HTCP bulk. b) High-resolution XPS spectra of Fe 2p for HTCP bulk and HTCP/MoS₂ heterostructures (5 and 15 cycles on 1T MoS₂, and 5 and 10 cycles on 2H MoS₂). GIXRD patterns of the MoS₂ heterostructure in c) the out-of-plane region and d) in-plane region.

in shape and peak position.^[24,49,50] The first band of the Fe 2p_{3/2} region located at ≈ 709.8 eV (olive green) is attributed to the main signal of Fe²⁺. The second at ≈ 711.2 eV (orange) comes from a mixture of multiplet splitting signals of the Fe²⁺ and Fe³⁺ species (see Table S4, Supporting Information). The third at ≈ 714.5 eV is caused by the multiplet splitting of the Fe²⁺, Fe³⁺, and Fe²⁺ satellite (pink) peaks. Unfortunately, this proximity makes it impossible to separate and quantify both contributions. However, a clear trend in the different heterostructures is observed. 1) The orange band area, caused by Fe³⁺ and Fe²⁺ contributions, decreases with the number of cycles. Therefore, the amount of Fe³⁺ decreases as the HTCP thickness increases. 2) The HTCP grown on 1T MoS₂ exhibits a less intense orange band, thus less Fe³⁺ population. 3) In the heterostructures, a new band located at ≈ 717 eV (gray) appears, which is the satellite peak of Fe³⁺, and follows the same trend as the orange band, decreasing for the thicker HTCP films (a ca. 2% for the x5 and x15 1T heterostructures, and a ca. 10% for x5 and x10 2H).^[49] Therefore, we can conclude that, on the one hand, the first layers of HTCP contain a higher amount of Fe³⁺, probably due to their low dimensionality, which facilitates Fe²⁺ oxidation when exposed to air after the LbL growth. On the other hand, the HTCP grown on 1T MoS₂ is less susceptible to oxidation. This agrees with our previous hy-

pothesis that the 1T MoS₂ acts as an electron donor, hence preventing the Fe²⁺ film from oxidizing. The Fe:Pt ratio was quantified for the different samples and was found to be around 0.9 for the 1T heterostructures and 1.1 for the 2H hybrids, which is reasonably close to the theoretical value of 1 (Table S5, Supporting Information). For the proper interpretation of these results, it is important to remark that all samples with a different number of layers were prepared simultaneously in separate substrates and then exposed to air for XPS measurements. Once a sample is removed from the glove box, no further HTCP growth is performed.

Next, by means of GIXRD, we explore the HTCP crystallinity in the heterostructures. Figure 4c,d show the out-of-plane and in-plane profiles of HTCP/1T and HTCP/2H with 30 layers, respectively, obtained from the area detector images (Figure S34, Supporting Information). The most intense diffraction peaks of the individual components of the heterostructures, MoS₂ and HTCP, are visible for all the heterostructures. The 020 and 040 diffraction peaks of the HTCP are present in the out-of-plane patterns, while the 002, 200, and 202 are present in the in-plane ones for both heterostructures. This indicates that the HTCP layers grow oriented with the *ab* planes parallel to the substrate. A small 111 peak can also be detected in the in-plane diffractograms

coming from the slight tilt of the HTCP layers with respect to the substrate plane, as previously observed for films grown on Au.^[11,12] Remarkably, MoS₂ flakes impose the same crystalline orientation as substrates functionalized with a py-terminated SAM.^[11,12]

Regarding the diffraction patterns of bare 2H and 1T MoS₂ networks, the only peaks present are those related to the 00l reflections, which only appear in out-of-plane diffraction patterns. This is indicative of all MoS₂ flakes laying parallel to the surface of the SiO₂. Noticeably, in the 1T phase, the main diffraction peak 001 corresponds to a ≈ 10 Å interlayer distance, which can be related to the presence of trapped water molecules between restacked MoS₂ layers during the 1T MoS₂ deposition. The second far less intense 002 peak corresponds to ≈ 6.2 Å interlayer space, which can be indicative of the presence of non-intercalated material (a similar diffraction pattern can be observed for a powder sample of 1T MoS₂, see Figure S35, Supporting Information). After the HTCP growth, both 001 and 002 peaks are preserved, and only the 001 peak is slightly shifted to higher *q* values, pointing to a decrease in the interlayer distance regarding the 1T MoS₂ powder, probably due to the presence of the coordination polymer. These results confirm not only the crystallinity of both components in the heterostructure but also their relative orientation with respect to each other. This is indicative of the substrate registry effect of the MoS₂ flakes on the growth of the HTCP. Thus, we analyzed the lattice mismatch between the *ac* plane of the HTCP and the *ab* planes of the 1T and 2H MoS₂ (see Figures S36 and S37, Supporting Information). Our findings indicate a mean mismatch of 4–16%, which is compatible with the MoS₂ exercising a substrate registry effect on the HTCP growth, even if the first layer may be defective. This is compatible with lattice mismatches previously observed for other heterostructures based on coordination polymers.^[51,52] More information is present in the lattice mismatch section in the Supporting Information. Furthermore, we have analyzed the effect of HTCP anchoring in the in-plane structure of MoS₂ by means of high-resolution transmission electron microscopy (HR-TEM) in a HTCP(*x*2)/1T sample. As shown in Figures S38–S40 (Supporting Information), the 1T MoS₂ flakes present the 1T' (distorted 1T) superstructure (in-plane *d*-spacing of 0.57 ± 0.01 nm) and is slightly impacted by the HTCP growth, expanding to 0.61 ± 0.02 nm.^[53,54] This shows that even while the MoS₂ is under stress from the HTCP growth, the effect at the interface is relatively small and entirely compatible with the lattice mismatch that the HTCP can withstand.

2.3. Study of the Spin Transition in the HTCP/MoS₂ Heterostructures

Once the proper formation and crystallinity of the HTCP on the heterostructures have been proved, we target to determine quantitatively the amount of Fe³⁺ and the number of Fe²⁺ centers susceptible to switch their spin state thermally. Usually, these studies are done by SQUID magnetometry like for the HTCP bulk sample, which presents a HS configuration at 300 K with a transition to LS at 208 K during cooling and a thermal hysteresis of 33 K. Here, due to the reduced amount of HTCP in the HTCP/MoS₂ heterostructures and the high diamagnetic contribution coming from the substrate, SQUID measurements could not be carried

out properly for heterostructures below 60 layers, presenting a similar thermal transition than the bulk material (Figure S41, Supporting Information). Instead, we can follow the Fe L_{2,3} absorption edges by XAS since these are extremely sensitive to Fe oxidation and spin states, changing their shape and intensity (Figure 5a). At this point, it is important to remark that the focus of the present study was not to precisely determine the variation of the spin transition temperature but to evaluate the completeness of the SCO transition itself (i.e., the number of Fe²⁺ centers able to change from HS to LS configuration). Therefore, due to the high demand for beamtime and mandated energy-saving restrictions, we did not perform scanning temperature XAS measurements, and experiments were only carried out at two temperatures, far from the spin transition temperature on both ends (i.e., 100 K and 300 K) looking for an effective spin transition in our samples.

Focusing on XAS measurements, first, we study the percentage of Fe³⁺ at 300 K as a function of the number of HTCP layers (Figure 5b). The ratio is estimated by fitting the L_{2,3} edges of each sample between 705 eV and 725 eV to a linear combination of HTCP in bulk at 300 K (Fe²⁺ HS), at 100 K (Fe²⁺ LS) and Fe³⁺, used as references (Figure S42, Supporting Information). The results of the deconvolution can be seen in Figures S43–S53 (Supporting Information). The percentage of Fe³⁺ at 300 K sharply decreases as the number of HTCP layers increases for both heterostructures, reaching leveling values of 8% (1T) and ca. 14% (2H) for *x* larger than 10–15 layers, (Figure 5b). The same trend is observed at 100 K (Figure S54, Supporting Information), supporting a good estimate of the Fe contributions. These results further support the role played by the 1T polytype in minimizing the Fe²⁺ oxidation at the interface due to its electron donor character.

Subsequently, we measured the Fe L_{2,3} edge at 300 K and 100 K to corroborate the spin transition. The spin state can be easily determined by looking at the changes experienced at the Fe L-edge. For instance, in heterostructures with *x* = 15 layers the measurements at 100 K of the two polytypes show a decrease in the A and A' peaks at the expense of the B and B' peaks (Figure 5a). This thermal response is in good agreement with the HTCP behavior in bulk (Figure S41b, Supporting Information). It points out the predominance of Fe²⁺ LS at 100 K and of Fe²⁺ HS at 300 K.^[12,55–57] Then, we estimate the amount of Fe²⁺ LS at 100 K with respect to the total amount of Fe²⁺. This corresponds to the fraction of Fe²⁺ centers susceptible to switching their spin state. As Figure 5c shows, the Fe²⁺ LS content sharply increases with the number of layers, *x*, until it stays relatively constant for *x* > 10 in both 1T and 2H heterostructures. The influence of the MoS₂ polytype is reflected in the higher Fe²⁺ LS contribution exhibited at 100 K by the 1T heterostructures. Interestingly, this Fe²⁺ LS fraction is detectable even in the case of 5 HTCP layers (4 nm) for the 1T heterostructures, while for the 2H heterostructure, no signal of Fe²⁺ LS is detected for this thickness. This difference can stem from the larger amount of oxidized Fe³⁺ found near the MoS₂ surface in the 2H heterostructures, blocking a more effective HTCP growth (Figure 5b). Hence, the more efficient spin transition in the 1T heterostructures is attributed to the negative charges that originate during MoS₂ chemical exfoliation. Therefore, it is highly recommended to ensure their presence by Z-potential measurements (Figure S1b, Supporting Information)

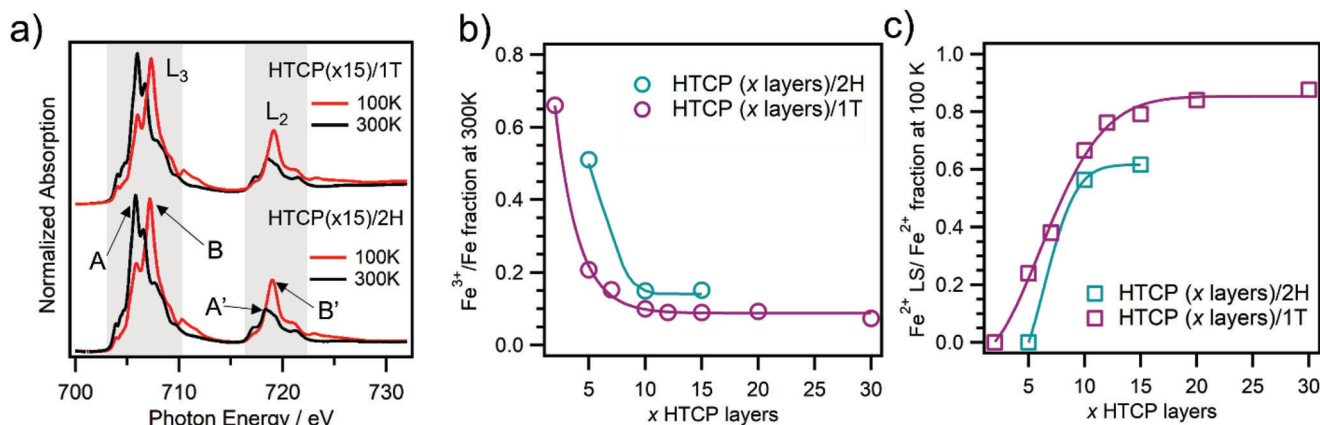


Figure 5. Study of the spin transition in the HTCP/MoS₂ heterostructures: a) Fe L_{2,3} XAS spectra of the 2H and 1T heterostructures with 15 HTCP layers at 100 K (red) and 300 K (black). b) Fraction of Fe³⁺ respect to all Fe at 300 K versus the number of HTCP layers in the heterostructure. The continuous lines are a guide for the eye. c) Fe²⁺ LS fraction respect to Fe²⁺ at 100 K for the 1T heterostructures and 2H heterostructures. The continuous lines are a guide for the eye.

of the flakes in suspension and work with freshly prepared samples under an inert atmosphere.

Finally, we have also explored whether the spin transition affects the MoS₂ properties in the heterostructures. To do that we monitored the S K-edge and the Mo K-edge EXAFS as a function of the temperature. As shown in Figures S24, S25, and S55–S60 (Supporting Information), no significant effect could be observed between 300 K and 100 K in any heterostructure (see more information in the EXAFS section in the Supporting Information). Therefore, we can conclude that, in this case, the spin transition of the HTCP does not couple with the MoS₂ physical properties. This is not surprising since the MoS₂ surface strongly influences the early stage of the HTCP growth process leading to an interfacial region (few nanometers thick) in which most Fe centers do not undergo a spin transition, thus minimizing any possible strain effects coming from the SCO component. Oxidized Fe centers and/or S defects produced during the chemical exfoliation process could be the origin of spin transition block.

3. Conclusion

We have developed a LbL protocol for selectively growing SCO coordination polymers onto MoS₂ monolayers. In particular, we have grown the SCO HTCP [Fe(py)₂{Pt(CN)₄}] on chemically exfoliated 1T (metallic) and 2H (semiconducting) MoS₂ layers. In these Janus-like asymmetric SCO/2D heterostructures, the thickness of the HTCP film can be accurately controlled thanks to the LbL approach. This bottom-up method results in the formation of crystalline and oriented ultrathin films of HTCP that, in contrast to conventional substrates such as Au, can be directly grown on the 2D material without the need of having a SAM-functionalized interface. This straightforward approach can present several advantages versus the use of presynthesized SCO crystals or nanoparticles, such as a complete coverage and homogeneous distribution of the SCO material. Hence, it should facilitate the fabrication of nanodevices based on these hybrid heterostructures. Furthermore, XAS, XPS, and EXAFS characterization revealed the influence of the nature of the 2D material over the SCO properties. Thus, while the negatively charged

1T MoS₂ metallic layer acts as a reducing agent and prevents the Fe²⁺ oxidation, a significant amount of oxidized Fe³⁺ centers are detected in the interfacial region near the 2H MoS₂ surface. This strongly influences the nucleation and growth of the HTCP in the early stages of the LbL process, by reducing the thickness of the inactive layer placed between the Fe²⁺ SCO network and the 1T MoS₂ layer to 4 nm (5 layers). In the 2H heterostructure, this inactive layer increases to ca. 8 nm due to the lower amount of Fe²⁺ centers near the interface. Overall, our observations prove the active role played by the 2D material in tuning the SCO performance of these hybrid heterostructures, thanks to its control over the growing of the SCO coordination polymer on the MoS₂ surface.

4. Experimental Section

Preparation of the Network of 1T MoS₂ Flakes: The aqueous suspended solution of MoS₂ flakes was prepared following the well-known method of *n*-BuLi intercalation.^[38] The quality of the exfoliated material was evaluated by powder X-ray diffraction (PXRD), Raman spectroscopy, XPS, and AFM. Flakes of MoS₂ (20 mm) were deposited onto SiO₂ by spin-coating at 50 rps. These optimized parameters assure a great covered area of 1T MoS₂ flakes without agglomeration of material as followed by AFM.

Conversion to 2H MoS₂ Phase: After spin-coating, substrates of 1T MoS₂ flakes were heated for 1 h at 200 °C under an Ar atmosphere to prevent air oxidation and allow conversion to the semiconducting 2H phase. Conversion to the 2H phase was confirmed by Raman spectroscopy and XPS.

Synthesis of HTCP/MoS₂ Hybrid Heterostructures: Ultrathin films of [Fe(py)₂{Pt(CN)₄}] were grown onto the different MoS₂ networks of flakes using a modified version of a previously reported LbL procedure. Using an automatized dipping robot, MoS₂-covered substrates were sequentially soaked in alternate ethanol solutions of 10 × 10⁻³ M Fe(BF₄)₂/100 × 10⁻³ M py and 10 × 10⁻³ M (TBA)₂Pt(CN)₄/100 × 10⁻³ M py with intermediate ethanol washing steps in a nitrogen-filled glovebox to prevent Fe²⁺ oxidation.

Supporting Information

Supporting Information is available from the Wiley Online Library or from the author.

Acknowledgements

This work was supported by the EU (ERC AdG Mol-2D 788222, FET OPEN SINFONIA 964396), the Spanish MCIN (Grants PID2020-117152RB-I00, PID2020-117264GB-I00 and CEX2019-000919-M funded by MCIN/AEI/10.13039/501100011033), the Generalitat Valenciana (PROMETEO Program and PO FEDER Program IDIFEDER/2021/078) and the French National Research Agency ANR (ANR-17-CE24-0004). A.N.-L. thanks the Spanish MECED for a FPU predoctoral fellowship (FPU16/02220). R.T.-C. thanks the Generalitat Valenciana for his APOSTD Fellowship (CIAPOS/2021/269). M.M.-G. thanks MCIN for a Margarita Salas Fellowship (MS21-041) with funding from European Union NextGenerationEU. N.V. thanks Generalitat Valenciana for her predoctoral fellowship GRISOLIAP/2019/030. V.R.-G. thanks the Research Foundation Flanders (FWO Vlaanderen) for a Junior Postdoctoral Fellowship (1263622N). S.T. thanks the Spanish MINECO for his Ramón y Cajal Fellowship (RYC-2016-19817). Experiments were performed on the DEIMOS and SAMBA beamlines at SOLEIL Synchrotron, France (proposal number 20181583 and 20191609). The authors are grateful to Florian Leduc for assistance in using DEIMOS beamline and to the SOLEIL staff for smoothly running the facility. The research leading to this result has been supported by the project CALIPSOplus under Grant Agreement 730872 from the EU Framework Programme for Research and Innovation HORIZON 2020. The authors gratefully acknowledge DELTA Dortmund synchrotron for allocation of beamtime at beamline BL9. The authors also thank Ángel López-Muñoz and Isaac Brotons for their technical support. This study forms part of the Advanced Materials program and was supported by MCIN with funding from European Union NextGenerationEU (PRTR-C17.11) and by Generalitat Valenciana. The authors acknowledge the use of instrumentation as well as the technical advice provided by the National Facility ELECMI ICTS node "Laboratorio de Microscopías Avanzadas" at the University of Zaragoza.

Conflict of Interest

The authors declare no conflict of interest.

Data Availability Statement

The data that support the findings of this study are available from the corresponding author upon reasonable request.

Keywords

2D heterostructures, Janus heterostructures, molybdenum disulfide, spin-crossover, transition metal dichalcogenides

Received: June 12, 2023

Revised: July 20, 2023

Published online:

- [1] A. Hauser, *Angew. Chem., Int. Ed.* **2013**, *52*, 10419.
- [2] J. Dugay, M. Giménez-Marqués, W. J. Venstra, R. Torres-Cavanillas, U. N. Sheombarsing, N. Manca, E. Coronado, H. S. J. Van Der Zant, *J. Phys. Chem. C* **2019**, *123*, 6778.
- [3] J. Dugay, W. Evers, R. Torres-Cavanillas, M. Giménez-Marqués, E. Coronado, H. S. J. Van Der Zant, *J. Phys. Chem. Lett.* **2018**, *9*, 5672.
- [4] R. Torres-Cavanillas, L. Lima-Moya, F. D. Tichelaar, H. W. Zandbergen, M. Giménez-Marqués, E. Coronado, *Dalton Trans.* **2019**, *48*, 15465.

- [5] G. Molnár, S. Rat, L. Salmon, W. Nicolazzi, A. Bousseksou, *Adv. Mater.* **2018**, *30*, 1703862.
- [6] F. Prins, M. Monrabal-Capilla, E. A. Osorio, E. Coronado, H. S. J. Van Der Zant, *Adv. Mater.* **2011**, *23*, 1545.
- [7] A. Rotaru, J. Dugay, R. P. Tan, I. A. Gural'skiy, L. Salmon, P. Demont, J. Carrey, G. Molnár, M. Respaud, A. Bousseksou, *Adv. Mater.* **2013**, *25*, 1745.
- [8] V. Rubio-Giménez, S. Tatay, C. Martí-Gastaldo, *Chem. Soc. Rev.* **2020**, *49*, 5601.
- [9] V. Niel, J. M. Martínez-Agudo, M. C. Muñoz, A. B. Gaspar, J. A. Real, *Inorg. Chem.* **2001**, *40*, 3838.
- [10] K. Otsubo, T. Haraguchi, H. Kitagawa, *Coord. Chem. Rev.* **2017**, *346*, 123.
- [11] S. Sakaida, K. Otsubo, O. Sakata, C. Song, A. Fujiwara, M. Takata, H. Kitagawa, *Nat. Chem.* **2016**, *8*, 377.
- [12] V. Rubio-Giménez, C. Bartual-Murgui, M. Galbiati, A. Núñez-López, J. Castells-Gil, B. Quinard, P. Seneor, E. Otero, P. Ohresser, A. Cantarero, E. Coronado, J. A. Real, R. Mattana, S. Tatay, C. Martí-Gastaldo, *Chem. Sci.* **2019**, *10*, 4038.
- [13] K. S. Kumar, M. Ruben, *Angew. Chem., Int. Ed.* **2021**, *60*, 7502.
- [14] T. G. Gopakumar, F. Matino, H. Naggert, A. Bannwarth, F. Tuczek, R. Berndt, *Angew. Chem., Int. Ed.* **2012**, *51*, 6262.
- [15] T. G. Gopakumar, M. Bernien, H. Naggert, F. Matino, C. F. Hermanns, A. Bannwarth, S. Mühlenberend, A. Krüger, D. Krüger, F. Nickel, W. Walter, R. Berndt, W. Kuch, F. Tuczek, *Chem. - Eur. J.* **2013**, *19*, 15702.
- [16] S. Ossinger, H. Naggert, L. Kipgen, T. Jasper-Toennies, A. Rai, J. Rudnik, F. Nickel, L. M. Arruda, M. Bernien, W. Kuch, R. Berndt, F. Tuczek, *J. Phys. Chem. C* **2017**, *121*, 1210.
- [17] X. Zhang, T. Palamarcic, J. François Létard, P. Rosa, E. V. Lozada, F. Torres, L. G. Rosa, B. Doudin, P. A. Dowben, *Chem. Commun.* **2014**, *50*, 2255.
- [18] A. Holovchenko, J. Dugay, M. Giménez-Marqués, R. Torres-Cavanillas, E. Coronado, H. S. J. van der Zant, *Adv. Mater.* **2016**, *28*, 7228.
- [19] J. Dugay, M. Aarts, M. Gimenez-Marqués, T. Kozlova, H. W. Zandbergen, E. Coronado, H. S. J. Van Der Zant, *Nano Lett.* **2017**, *17*, 186.
- [20] E. P. van Geest, K. Shakouri, W. Fu, V. Robert, V. Tudor, S. Bonnet, G. F. Schneider, *Adv. Mater.* **2020**, *32*, 1903575.
- [21] C. Boix-Constant, V. García-López, E. Navarro-Moratalla, M. Clemente-León, J. L. Zafra, J. Casado, F. Guinea, S. Mañas-Valero, E. Coronado, *Adv. Mater.* **2022**, *34*, 2110027.
- [22] N. Konstantinov, A. Tauzin, U. N. Noubé, D. Dragoe, B. Kundys, H. Majjad, A. Brosseau, M. Lenertz, A. Singh, S. Berciaud, M. L. Boillot, B. Doudin, T. Mallah, J. F. Dayen, *J. Mater. Chem. C* **2021**, *9*, 2712.
- [23] M. Gavara-Edo, R. Córdoba, F. J. Valverde-Muñoz, J. Herrero-Martín, J. A. Real, E. Coronado, *Adv. Mater.* **2022**, *34*, 2202551.
- [24] R. Torres-Cavanillas, M. Morant-Giner, G. Escorcía-Ariza, J. Dugay, J. Canet-Ferrer, S. Tatay, S. Cardona-Serra, M. Giménez-Marqués, M. Galbiati, A. Forment-Aliaga, E. Coronado, *Nat. Chem.* **2021**, *13*, 1101.
- [25] I. Brotons-Alcázar, R. Torres-Cavanillas, M. Morant-Giner, M. Cvikl, S. Mañas-Valero, A. Forment-Aliaga, E. Coronado, *Dalton Trans.* **2021**, *50*, 16281.
- [26] V. Shanmugam, R. A. Mensah, K. Babu, S. Gawusu, A. Chanda, Y. Tu, R. E. Neisiany, M. Först, G. Sas, O. Das, *Part. Part. Syst. Charact.* **2022**, *39*, 2200031.
- [27] Q. Huang, X. Li, M. Sun, L. Zhang, C. Song, L. Zhu, P. Chen, Z. Xu, W. Wang, X. Bai, *Adv. Mater. Interfaces* **2017**, *4*, 1700171.
- [28] X. Zhang, Z. Lai, C. Tan, H. Zhang, *Angew. Chem., Int. Ed.* **2016**, *55*, 8816.
- [29] Y. Huang, J. Guo, Y. Kang, Y. Ai, C. M. Li, *Nanoscale* **2015**, *7*, 19358.
- [30] K. F. Mak, C. Lee, J. Hone, J. Shan, T. F. Heinz, *Phys. Rev. Lett.* **2010**, *105*, 2.

- [31] Z. He, W. Que, *Appl. Mater. Today* **2016**, 3, 23.
- [32] W. Zhao, J. Pan, Y. Fang, X. Che, D. Wang, K. Bu, F. Huang, *Chem. - Eur. J.* **2018**, 24, 15942.
- [33] A. Hirsch, F. Hauke, *Angew. Chem., Int. Ed.* **2018**, 57, 4338.
- [34] F. H. L. Koppens, T. Mueller, P. Avouris, A. C. Ferrari, M. S. Vitiello, M. Polini, *Nat. Nanotechnol.* **2014**, 9, 780.
- [35] X. Xu, W. Yao, D. Xiao, T. F. Heinz, *Nat. Phys.* **2014**, 10, 343.
- [36] R. Dong, I. Kuljanishvili, J. Vac, *Sci. Technol., B: Nanotechnol. Microelectron.: Mater., Process., Meas., Phenom.* **2017**, 35, 030803.
- [37] L. Zhang, Z. Yang, T. Gong, R. Pan, H. Wang, Z. Guo, H. Zhang, X. Fu, *J. Mater. Chem. A* **2020**, 8, 8813.
- [38] L. Zhou, B. He, Y. Yang, Y. He, *RSC Adv.* **2014**, 4, 32570.
- [39] G. Eda, H. Yamaguchi, D. Voiry, T. Fujita, M. Chen, M. Chhowalla, *Nano Lett.* **2011**, 11, 5111.
- [40] V. Rubio-Giménez, S. Tatay, F. Volatron, F. J. Martínez-Casado, C. Martí-Gastaldo, E. Coronado, *J. Am. Chem. Soc.* **2016**, 138, 2576.
- [41] S. Park, T. Schultz, X. Xu, B. Wegner, A. Aljarb, A. Han, L. J. Li, V. C. Tung, P. Amsalem, N. Koch, *Commun. Phys.* **2019**, 2, 109.
- [42] S. H. Zhou, C. W. Zhou, X. D. Yang, Y. Li, J. Q. Zhong, H. Y. Mao, *Chin. Phys. Lett.* **2021**, 38, 057305.
- [43] D. Li, G. M. Bancroft, M. Kasrai, M. E. Fleet, X. H. Feng, K. H. Tan, *Phys. Chem. Miner.* **1995**, 22, 123.
- [44] L. Noodleman, J. G. Norman, J. H. Osborne, A. Aizman, D. A. Case, *J. Am. Chem. Soc.* **1985**, 107, 3418.
- [45] L. shan Kau, D. J. Spira-solomon, J. E. Spira-solomon-penner-hahn, K. O. Hodgson, E. I. Solomon, *J. Am. Chem. Soc.* **1987**, 109, 6433.
- [46] M. Kulichenko, A. I. Boldyrev, *J. Phys. Chem. C* **2020**, 124, 6267.
- [47] M. Krbal, V. Prokop, A. A. Kononov, J. R. Pereira, J. Mistrik, A. V. Kolobov, P. J. Fons, Y. Saito, S. Hatayama, Y. Shuang, Y. Sutou, S. A. Rozhkov, J. R. Stellhorn, S. Hayakawa, I. Pis, F. Bondino, *ACS Appl. Nano Mater.* **2021**, 4, 8834.
- [48] M. L. Greenfield, M. Byrne, S. Mitra-Kirtley, E. M. Kercher, T. B. Bolin, T. Wu, P. R. Craddock, K. D. Bake, A. E. Pomerantz, *Fuel* **2015**, 162, 179.
- [49] R. Sanchis-Gual, R. Torres-Cavanillas, M. Coronado-Puchau, M. Giménez-Marqués, E. Coronado, *J. Mater. Chem. C* **2021**, 9, 10811.
- [50] L. Poggini, M. Gonidec, J. H. González-Estefán, G. Pecastaings, B. Gobaut, P. Rosa, *Adv. Electron. Mater.* **2018**, 4, 1800204.
- [51] K. Ikigaki, K. Okada, M. Takahashi, *ACS Appl. Nano Mater.* **2021**, 4, 3467.
- [52] J. Ha, H. R. Moon, *CrystEngComm* **2021**, 23, 2337.
- [53] K. Leng, Z. Chen, X. Zhao, W. Tang, B. Tian, C. T. Nai, W. Zhou, K. P. Loh, *ACS Nano* **2016**, 10, 9208.
- [54] K. Chrissafis, M. Zamani, K. Kambas, J. Stoemenos, N. A. Economou, I. Samaras, C. Julien, *Mater. Sci. Eng. B* **1989**, 3, 145.
- [55] M. Bernien, D. Wiedemann, C. F. Hermanns, A. Kruüger, D. Rolf, W. Kroener, P. Müller, A. Grohmann, W. Kuch, *J. Phys. Chem. Lett.* **2012**, 3, 3431.
- [56] V. Davesne, M. Gruber, M. Studniarek, W. H. Doh, S. Zafeiratos, L. Joly, F. Sirotti, M. G. Silly, A. B. Gaspar, J. A. Real, G. Schmerber, M. Bowen, W. Weber, S. Boukari, V. Da Costa, J. Arabski, W. Wulfhekel, E. Beaurepaire, *J. Chem. Phys.* **2015**, 142, 194702.
- [57] P. Ohresser, E. Otero, F. Choueikani, K. Chen, S. Stanescu, F. Deschamps, T. Moreno, F. Polack, B. Lagarde, J. P. Daguerré, F. Marteau, F. Scheurer, L. Joly, J. P. Kappler, B. Muller, O. Bunau, P. Saintavit, *Rev. Sci. Instrum.* **2014**, 85, 013106.